ACS OMEGA

http://pubs.acs.org/journal/acsodf

Article

Multistimulus-Responsive Supramolecular Hydrogels Derived by *in situ* Coating of Ag Nanoparticles on 5′-CMP-Capped β-FeOOH Binary Nanohybrids with Multifunctional Features and Applications

Priyanka and Anil Kumar*

Cite This: *ACS Omega* 2020, 5, 13672−13684

Read Online

ACCESS | Metrics & More | Article Recommendations | Supporting Information

ABSTRACT: The present manuscript reports the synthesis of multistimulus-responsive smart supramolecular hydrogels derived by *in situ* coating of silver nanoparticles (Ag NPs) on colloidal cytidine-5′-monophosphate-capped β-FeOOH nanohybrids (β-FeOOH@5′-CMP) under physiological conditions forming a polycrystalline building block (Ag-coated β-FeOOH@5′-CMP). The presence of Ag in the binary nanohybrids induces the puckering of ribose sugar, bringing a change in its conformation from C2′-endo to C3′-endo, which enhanced the supramolecular interactions among different moieties of other building blocks to construct a porous network of hydrogels in the self-assembly *via* the formation of a micellar structure. Such a supramolecular network in hydrogel is also evidenced by the reversible sol⇌gel transformation under multistimulus-responsiveness in a narrow range of pH, temperature, and sonication, as well as by the manifestation of rapid self-healing and injectability features. As-synthesized hydrogels exhibiting shear-thinning behavior under higher strain and converting back into the sol under low strain, suggests their potential for localized drug delivery. The presence of Ag NPs in the hydrogel enhanced its viscoelastic properties, % swelling (580) and loading capabilities (590 mg g^{-1}) for methylene blue (MB), and its controlled release over days (∼2−30) as a function of pH. It displayed excellent surface-enhanced Raman spectroscopy activity allowing to detect MB-like drug molecules at ≤10^{-12} M. Thus, the as-synthesized hydrogels represent a unique superparamagnetic nanosystem consisting of all greener components (5′-CMP/β-FeOOH/Ag) with superior viscoelastic, sensing, and antimicrobial properties, displaying multistimulus-responsiveness (pH/temperature/sonication), thereby suggesting their vast potential for biomedical and environmental applications.

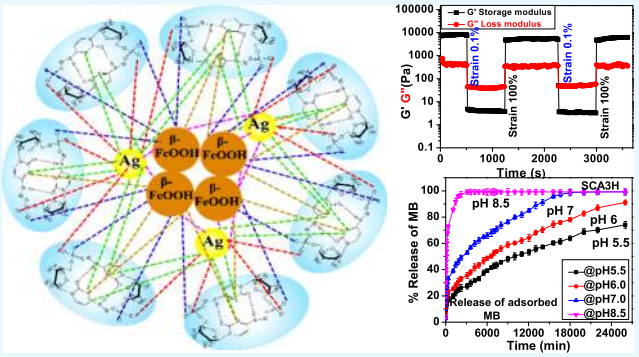

1. INTRODUCTION

In recent years, the fabrication of small molecule-based stimuli-responsive supramolecular hydrogels has been drawing increasing attention in which the 3D network is generally attained in the process of self-assembly involving noncovalent interactions.[1,2] The construction of the dynamic supramolecular hydrogels employing a low-molecular weight substrate has been considered as a novel alternative to synthetic covalently linked polymeric hydrogels because the synthesis of the latter often requires harsh conditions and multiple steps[3,4] besides being generally irreversible, lacking biocompatibility, self-healing, and injectability.[5−8] Molecular hydrogels consisting of natural biocompatible molecules, with large functional groups because of their relatively low cytotoxicity, are considered suitable for effective functional applications such as drug delivery, tissue engineering, wound healing, design of implant, and cosmetics because of their hydrophilicity, self-healing, injectability features, and complete reversibility upon being subjected to different physical or chemical stimuli.[9,10] The β-FeOOH phase, having a tunnel-like structure and being biodegradable with relatively low cytotoxicity, could provide a safe matrix for hydrogel.[11−13] The embedding of silver nanoparticles (Ag NPs) in such a hydrogel matrix could be safely utilized for further intensifying their biomedical applications because of their distinctive antimicrobial properties with low toxicity,[14] drug delivery, and sensing exploiting surface-enhanced Raman spectroscopy (SERS).[15−17] It, therefore, requires the development of new effective silver-encapsulated supramolecular hydrogel systems with improved characteristics.

The Food and Drug Administration (FDA) approved natural nucleotide molecules guanosine 5′-monophosphate (5′-GMP)/adenosine 5′-monophosphate (5′-AMP)/cytidine

Received: February 24, 2020
Accepted: May 21, 2020
Published: June 4, 2020

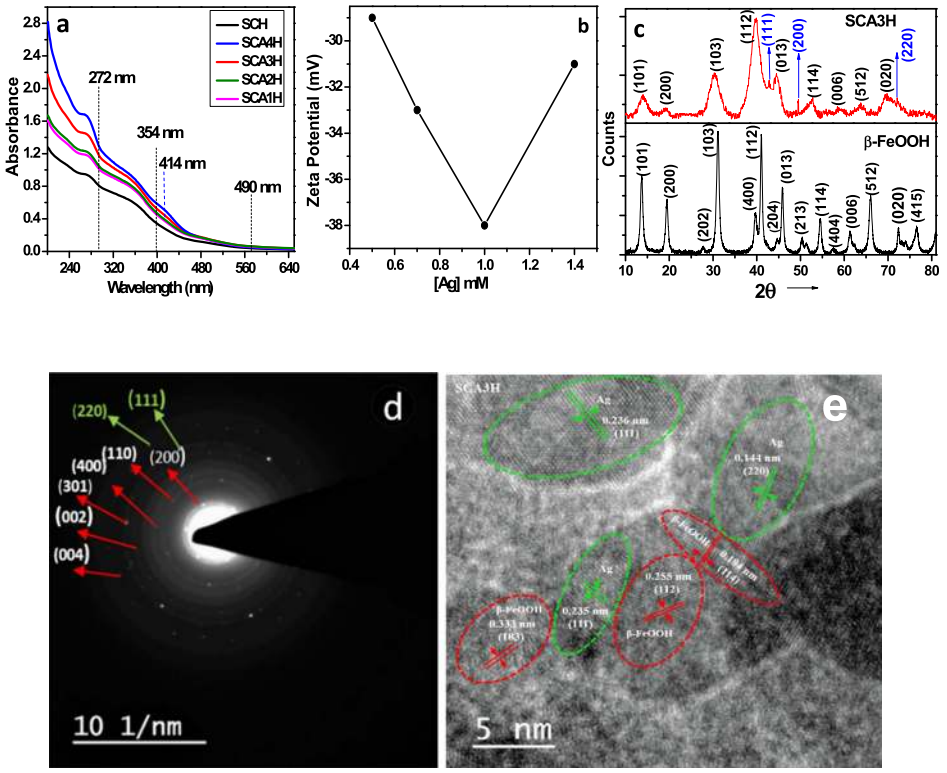

Figure 1. UV−vis spectra of hydrogel samples containing different [Ag] NPs along with hydrogel without Ag NPs (SCH) (panel a); zeta potential with different [Ag] NPs hydrogels (panel b); X-ray diffraction (XRD) of SCA3H along with bare β-FeOOH (panel c); SAED of SCA3H (panel d); and HRTEM of SCA3H (panel e).

5′-monophosphate (5′-CMP)/uridine 5′-monophosphate (5′-UMP), being the key components of the nucleic acids (RNA/DNA),[18,19] are known to participate in several important biological activities in living systems and display molecular recognition ability.[20] These molecules have been used to synthesize their coordination complexes with several transition-metal ions involving supramolecular interactions.[21,22] Such molecules might demonstrate tremendous potential for the fabrication of supramolecular gels for the above envisaged biomedical applications.[9,23−28] There are a few reports on the development of 5′-GMP/5′-AMP-based supramolecular hydrogels showing some of the hydrogel characteristics,[26,27] but with regards to employing pyrimidine-based nucleotide(s) (5′-CMP/5′-UMP) for synthesis of respective hydrogels, however, did not succeed even in the presence of certain ions such as lanthanides[26] and zinc.[27] Pyrimidine-based nucleotides mediated hydrogel formation though could serve as a missing building block in predicting the behavior of nucleic acid-based hydrogels. Recently, 5′-CMP-mediated soft supramolecular hydrogels upon its interaction with akaganeite is observed to provide a safe matrix for loading/release of drugs.[29] It though lacked in respects of their relatively poor loading/release capabilities, swelling, and sensing and antimicrobial features as compared to those designed using artificial molecule(s).[30]

In the present work, we report a facile synthesis of 5′-CMP-mediated multistimulus-responsive supramolecular hydrogels produced involving other less toxic biocompatible and inorganic components such as Ag and β-FeOOH *via* the formation of Ag-coated β-FeOOH@5′-CMP binary nanohybrids as its building block. The nanohybrids at pH 7.0 undergo rapid gelation in the self-assembly process (in <5 min) at room temperature (RT) and exhibited all characteristics of the soft supramolecular hydrogels such as physical and chemical stimulus-responsiveness, reversible transformation in a narrow range of pH and temperature, self-healing, and injectability. It depicted high % swelling (580) and efficient loading at pH 7.0 and slow controlled release of MB, besides showing low cytotoxicity and selective antimicrobial properties. The presence of Ag NPs in the porous hydrogel network exhibited excellent SERS activity, which is explored for the detection of MB. These distinctive features make as-synthesized hydrogels unique as compared to previously reported nucleotide-mediated supramolecular hydrogels.[31−33]

2. RESULTS

2.1. Optimization and Characterization of Hydrogel.

2.1.1. Effect of [Ag] on the Optical Spectrum of the 5′-CMP-β-FeOOH Hydrogel. The amount of Ag in the as-synthesized hydrogels has been optimized by recording the optical absorption spectra of the hydrogel samples containing varied amounts of Ag (mM) 0.5−1.4, and they are denoted as: SCA1H (0.5), SCA2H (0.7), SCA3H (1.0), and SCA4H (1.4) along with the bare 5′-CMP-β-FeOOH (SCH) (0.0) (Figure 1, panel a). The samples containing Ag exhibited four broadbands (nm) at around: 272, 354, 414, and 490 nm. The peaks (nm) at 272, 354, and ∼490 can be assigned to ligand based transition, ligand field transition, and Fe−Fe pair double excitation, respectively. The development of a new band at around 414 nm, the intensity of which grows with increasing Ag NPs unlike that obtained in the absence of silver NPs (SCH), which clearly suggests the development of a plasmonic band due to Ag NPs in these samples, as could be seen in their enlarged images shown in Figure S1A. Ag NPs were also produced using 5′-CMP as the template in the

https://dx.doi.org/10.1021/acsomega.0c00815
ACS Omega 2020, 5, 13672−13684

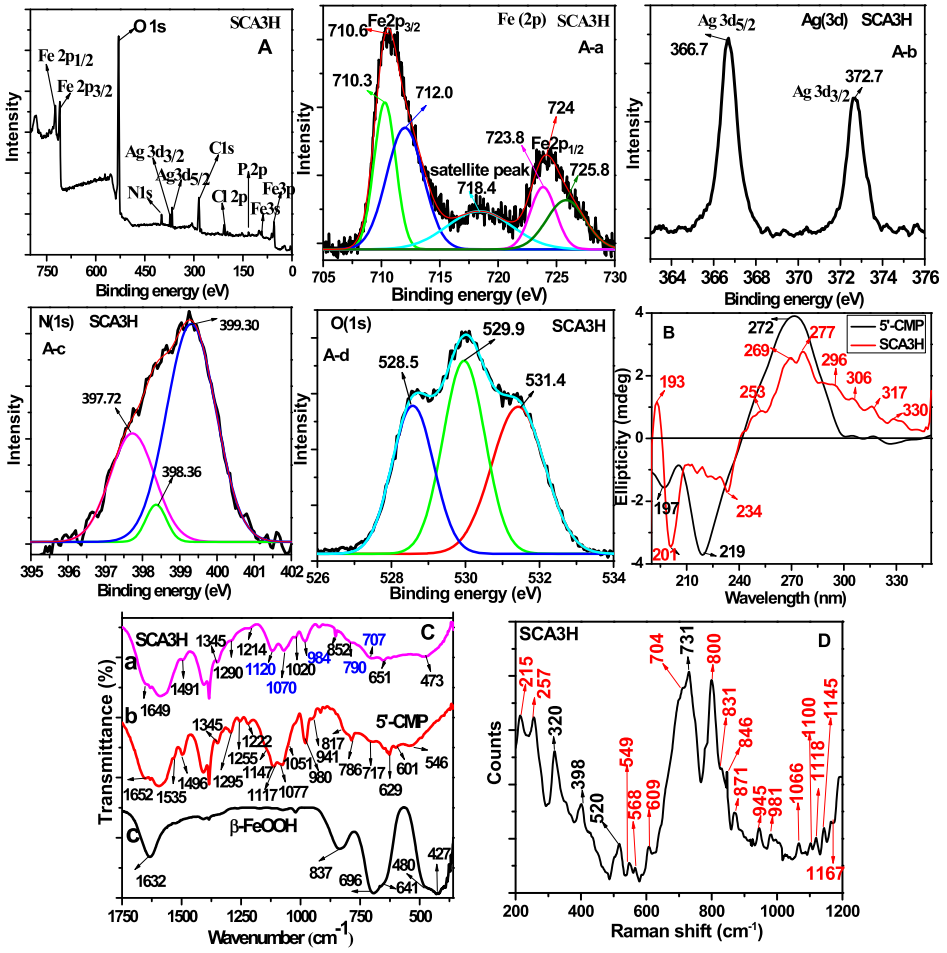

Figure 2. XPS spectra of SCA3H: survey scan (panel A); narrow range scans of—Fe (2p) (panel A-a); Ag (3d) (panel A-b), N (1s) (panel A-c), O (2s) (panel A-d); CD spectra of bare 5′-CMP and SCA3H (panel B); FTIR spectra of SCA3H (curve a), 5′-CMP (curve b) and *β*-FeOOH (curve c) in (panel C); and Raman spectrum of SCA3H (panel D).

absence of *β*-FeOOH. It also exhibited the surface plasmonic resonance band (SPR) around 410 nm (Figure S1B), which supports the formation of Ag NPs in SCAH samples. Further, an increasing *in situ* coating of Ag NPs on SCH red-shifted the band at 490 nm incrementally, whereas simultaneously the band at 354 nm is blue-shifted. The observed difference might have arisen because of a change in the particle size of Ag NPs upon increasing [Ag], which has been correlated earlier with a change in the electron affinity of these particles with size.[34] Among these samples, the time taken for gelation has been found to be the minimum for the sample containing 1 mM Ag NPs (SCA3H).

This aspect was further probed by recording the stability of these colloidal samples a by using dynamic light scattering (DLS) instrument. A variation in the value of zeta potential (ζ) as a function of change in the amount of Ag NPs in these samples at pH 7.0 is shown in Figure 1, panel b (Table S1). It exhibited the highest value of ζ for the sample containing 1 mM of Ag NPs (−38 mV), suggesting it to be the most stable.

The presence of different phase(s) in the binary nanohybrids was further analyzed by XRD (Figure 1, panel c). The XRD pattern due to SCA3H is found to correspond to the reflections from (101), (200), (103), (112), (013), (114), (006), (512), and (020) planes matching with the JCPDS file 80-1770 because of *β*-FeOOH having a monoclinic structure. A comparison of the XRD pattern of SCA3H with that of pure *β*-FeOOH shows that the peaks due to the *β*-FeOOH phase have now become relatively less intense, besides some of the peaks disappeared and several new peaks appeared at 2θ values of 44.6, 51.8, and 76.2. These reflections matched with the planes (111), (200), and (220) corresponding to the cubic phase of silver (JCPDS file 04-0783). The disappearance and a reduction in the intensity of some peaks due to the *β*-FeOOH phase in SCA3H is understandable because of their presence now in the hydrogel (SCA3H). The spots in selected area electron diffraction (SAED) pattern of SCA3H indicated it to be polycrystalline and indexing of these rings corresponded to both *β*-FeOOH and Ag NPs (Figure 1, panel d). High-resolution transmission electron microscopy (HRTEM) analysis of this sample also showed the *d* spacing (nm) of 0.255, 0.333, 0.194, 0.236, 0.144, and 0.235 matching with the (112), (103), (114), (111), (220), and (111) planes corresponding to *β*-FeOOH and Ag NPs, respectively (Figure 1, panel e). The prominence of these planes are also indicated from its XRD pattern (Figure 1, panel c).

The presence of the different elements and their environment in SCA3H was analyzed by X-ray photoelectron spectroscopy (XPS) in the 0−800 eV binding energy range. The survey scan spectrum of SCA3H reveals the presence of Fe (2p), Ag (3d), N (1s), O (2s), C (1s), P (2p), and Cl (2p) elements (Figure 2, panel A). Their high-resolution spectrum in the narrow binding energy range (Figure 2, panel A-a to A-d

https://dx.doi.org/10.1021/acsomega.0c00815
ACS Omega 2020, 5, 13672−13684

Scheme 1. (A) Interactions within the Building Block (Shown as A′) in SCA3; (B) Micellar Formation in SCA3H; (C) Supramolecular Interactions among Different Components in the Building Blocks

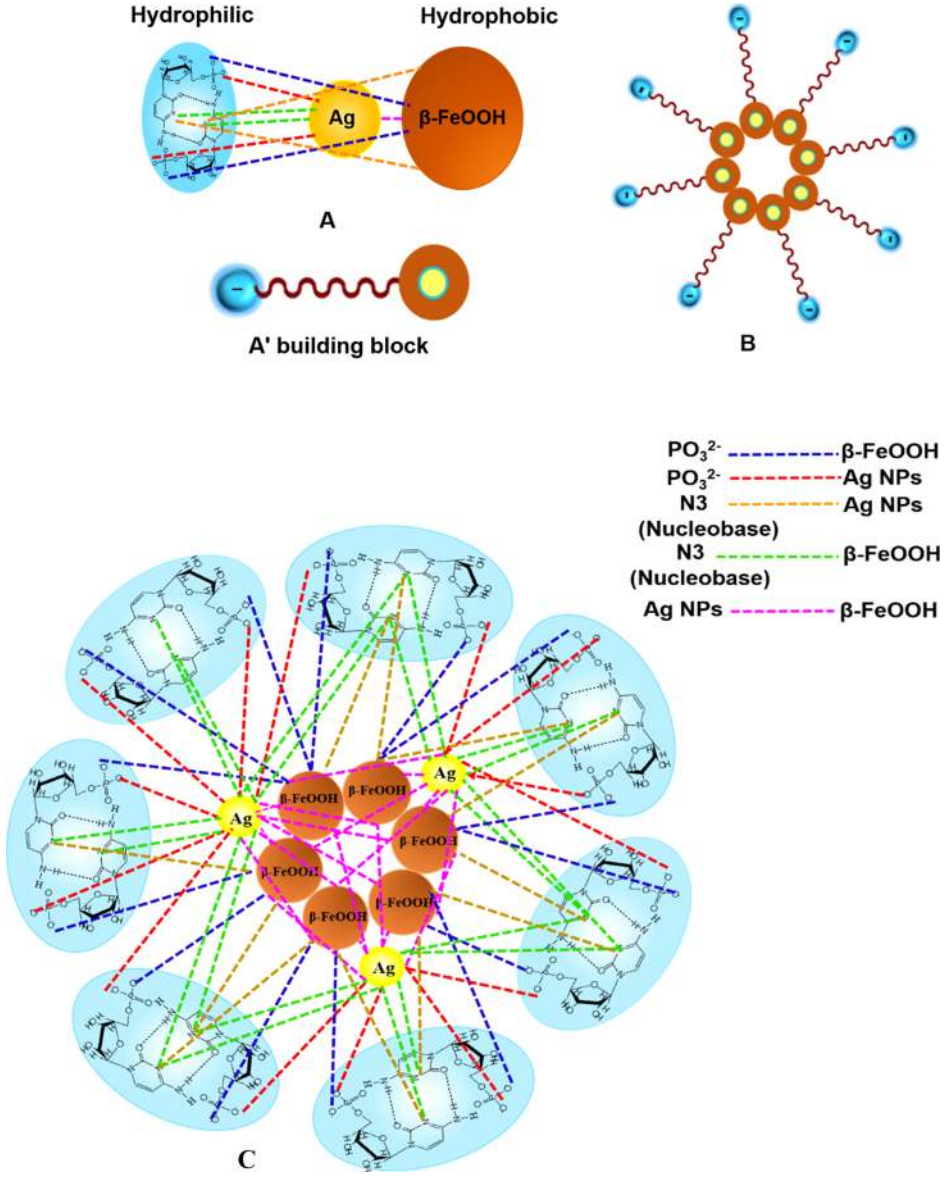

and Figure S2, Table S2) showed that the spectrum of the Fe element contains two bands at (eV) 710.6 and 724 corresponding Fe ($2p_{3/2}$) and Fe ($2p_{1/2}$), respectively, with a spin orbital coupling of 13.4 eV along with a satellite peak at 718.4 eV. The deconvolution of these bands showed the presence of four peaks and each pair exhibited a spin orbital coupling of 13.5 ± 0.3 eV. The Ag (3d) spectrum showed the two peaks at (eV) 366.7 and 372.7 corresponding to the $3d_{5/2}$ and $3d_{3/2}$ orbits of Ag (metallic silver) with a spin orbital coupling of 6 eV. However, these peaks were shifted to lower energy than that of the bulk,[35] suggesting the binding of Fe and Ag centers in SCA3H through noncovalent interactions with 5′-CMP.

Figure 2, panel B shows the CD spectra of bare 5′-CMP along with the SCA3H recorded under similar experimental conditions. The CD spectra of SCA3H exhibited several peaks with positive and negative ellipticity (nm) at: 193, 253, 269, 277, 296, 306, 317, and 330; and 201 and 234, respectively. In contrast, the CD spectrum due to bare 5′-CMP exhibited only a few peaks with positive and negative ellipticity (nm) at: 272; 219; and 197, respectively. These spectral changes clearly suggest a change in its chirality in the hydrogel sample, which might have increased supramolecular involving van der Waals and H-bonding interactions upon gelation, which results in new Π−Π*, n−Π* transitions arising from the pyrimidine rings.[21,36] The observed redshift in the vicinity of 272−300 nm may be assigned to Π−Π* transitions involving Π−Π stacking interactions, which might have resulted due to the clockwise rotation of sugar generating the P helix. The blueshift in the peak with negative ellipticity as compared to bare 5′-CMP suggests some hindrance in the n−Π* transitions causing a shift in these bands to higher energy, possibly arising because of the involvement of nonbonding electrons present on N3 for forming the dative bond with silver. The appearance of a new positive band at 193 nm suggests the involvement of electronic transitions in the supramolecular helical structure. Thus, the binding of Ag and Fe to 5′-CMP in SCA3H evidently suggests a change in its chirality.

https://dx.doi.org/10.1021/acsomega.0c00815
ACS Omega 2020, 5, 13672−13684

An interaction of different functional groups of bare 5′-CMP with inorganic components in SCA3H was further probed by recording its IR and Raman spectra (Figure 2, panel C and panel D; Tables S3 and S4). A comparison of IR spectra of bare 5′-CMP with that of SCA3H recorded under identical conditions of pH (Figure 2, panel C curve a and b) reveals that the peaks because of the following functional groups of 5′-CMP: cytosine bending mode, (δ N1−C1′−O4′), P−O str., ribose sugar in phase (δ C4′C5′H), ribose sugar (δ O3′C3′H), $-PO_3^{2-}$ deg., (δ C2′C1′H); r(NH2); (δ O1′C1′H), (δ N−H) in plane vanished completely; some of the peaks are red-shifted (cm^{-1}): from 717 to 707 (δ C5−C4−N4), 1222 to 1214 (δ C2′O2′H of RS), 1295 to 1286 (C + RS), 1496 to 1491 (δ C4═N3)/(C4−N4), 1657 to 1650 (C2═O2 str.); whereas, some peaks are blue-shifted (cm^{-1}): from 629 to 651 (δ C2′−Cl′−N1) and δ(Nl−Cl′−O4′), 786 to 790 (ring breathing), 980 to 984 ($-PO_3^{2-}$ sym. str.)/$-NH_2$ bending, and 1117 to 1120 (νC4′O−νC4′C3′−δ C3′O3′).[37] Apart from these, some new peaks appeared at (cm^{-1}): 852 (δ C2′−Cl′−O4′) and 1022 (RS). These changes clearly show a very effective interaction of β-FeOOH and Ag NPs with the functional groups of 5′-CMP. These interactions also influence the vibrational bands because of bare β-FeOOH (Table S3). Some of the peaks (cm^{-1}) because of β-FeOOH (427, 641, 696, 837, and 1632) in SCA3H get diminished; whereas, peak (cm^{-1}) at 480 is red-shifted to 473.

These interactions were further analyzed by Raman spectroscopy (Figure 2, panel D) which exhibited a red shift with an increase in intensity in the following peaks (cm^{-1}) due to 5′-CMP: 464 to 454 (C + RS), 554 to 550 (δ C2−N3═C4), and (δ N1−C2−N3), 629 to 624 (δ N1−C1′−O), 986 to 981 out of phase (δ C4−N4H)/(PO_3^{2-} str)., 1071 to 1066 (RS), and 1265 to 1250 (C + RS). Whereas, some of the peaks get blue-shifted (cm^{-1}): 586 to 609 (C2═O2 bending), 788 to 800 (ring breathing), 700 to 704 (C5−C4−N4), 842 to 846 (δ C2′−C1′−O), 941 to 945 (δ O3′−C3′H), 1096 to 1100 (RS), 1138 to 1145 (δ C2′C1′H); rNH_2; and (δ O1′C1′H), ν(C1′═N1). Apart from these, some new peaks (cm^{-1}) also appeared at 1118 (νC4′O−νC4′C3′−δC3′O3′) and 1300 (δ C2′−C1′). There is also a shift in the peaks (cm^{-1}) because of β-FeOOH in SCA3H from 322 to 320; 388 to 398 (Fe−O vib. of octahedral Fe site), 539 to 520, and 720 to 731.

The above observed changes in IR and Raman spectroscopy clearly show an interaction of 5′-CMP with Ag NPs and β-FeOOH. Ag might be involved in forming the dative bond with N3, $-NH_2$, and PO_3^{2-} of 5′-CMP and −OH of the β-FeOOH. The electrons in the dative bond are expected to have relatively lower binding energies, which is clearly supported by the observed changes in the binding energy(ies) due to silver in the XPS analysis (Figure 2, panel A-b). Similarly, the binding energies because of N, P, and O are also observed to decrease which might be involved in the formation of weak noncovalent interactions with Ag NPs, β-FeOOH, and different moieties of other building blocks (Figure 2, panel A-d) as compared to those noted in the absence of Ag.[29] Based on these observations, interactions among different components of the nanohybrids are shown in Scheme 1A (*vide infra*).

2.2. Properties. *2.2.1. Swelling.* The porosity of as-synthesized SCA3H was further probed by measuring the uptake of water as a function of time at RT in a PBS buffer of pH 7.0 [Figure 3 for both soft and FD (freeze dried)] gel. This figure clearly shows that the % swelling ratio is much higher for the soft gel (curve a) as compared to FD gel (curve b). The %

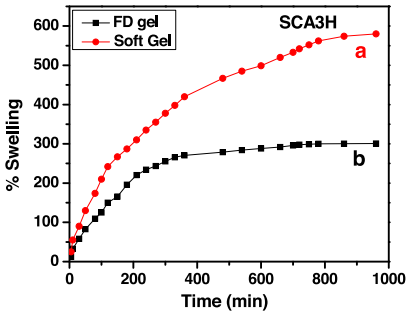

Figure 3. % Swelling of SCA3H soft (curve a) and FD (curve b) gel in PBS pH 7.0.

swelling in soft gel initially increases linearly and rapidly for up to about 100 min and, thereafter, it slowed down and took a plateau after about 800 min. The plateau value corresponds to a % swelling ratio of 580. This swelling behavior is quite different to that of FD gel which has about half the % swelling value attained in about 400 min only.

2.2.2. Viscoelastic Measurements. The effect of the amount of Ag in the hydrogel was further optimized by monitoring the viscosity as a function of time and shear rate, and oscillatory sweep measurements for different samples (Figures 4 and S3). Among all these samples, the highest viscosity at a fixed shear rate (100 s^{-1}) (Figure 4, panel A) as well as its slow decay as a function of shear rate (Figure S3A) indicates its hydrogel nature.

An examination of oscillatory sweep measurements (Figure 4, panel B) shows SCA3H to have excellent rheological features, such as storage modulus (36,947 Pa), loss modulus (3491 Pa), yield strain (15.2%), and linear viscoelastic region (LVR) (5.0%), among all the samples (Table S5). The stability of hydrogel in the LVR range is also supported by monitoring G' and G'' versus angular frequency (ω) at constant strain (0.5%) (Figure S3B), which demonstrated them to be almost constant in the entire recorded angular frequency range. Further, a plot of variation of storage modulus (G') and loss modulus (G'') as a function of the change in shear stress at a fixed frequency (1 Hz) also shows the highest mechanical stability up to 534 Pa for SCA3H (Figure 4, panel C), clearly supporting the above observations.

2.2.3. Self-Healing and Injectability. The self-healing nature of the as-synthesized hydrogel were proved by cutting it into two pieces and, thereafter, putting them back together without applying any external force. It is observed to heal within a few minutes (Figure 4, panel D). The sol−gel transformation, as was revealed by rheological measurements (Figure 4), was also tested qualitatively by taking the hydrogel in a syringe which under mild mechanical force undergoes transformation into the sol by breaking the supramolecular bond. This sol could be used to write on a glass slide and is reformed quickly into the gel as the mechanical force was removed.

The self-healing and injectable features of the hydrogel were also analyzed quantitatively by performing thixotropic measurements, in which G' and G'' were performed as a function of time at 0.1 and 100% strain at a constant frequency. At lower strain value, it showed the storage modulus to be greater than the loss modulus indicating the presence of gel. When the strain is increased to 100%, it resulted in a reversal of G' and G'' values, suggesting the transformation of the hydrogel into sol (Figure 4, panel E) possibly by breaking the

https://dx.doi.org/10.1021/acsomega.0c00815
ACS Omega 2020, 5, 13672−13684

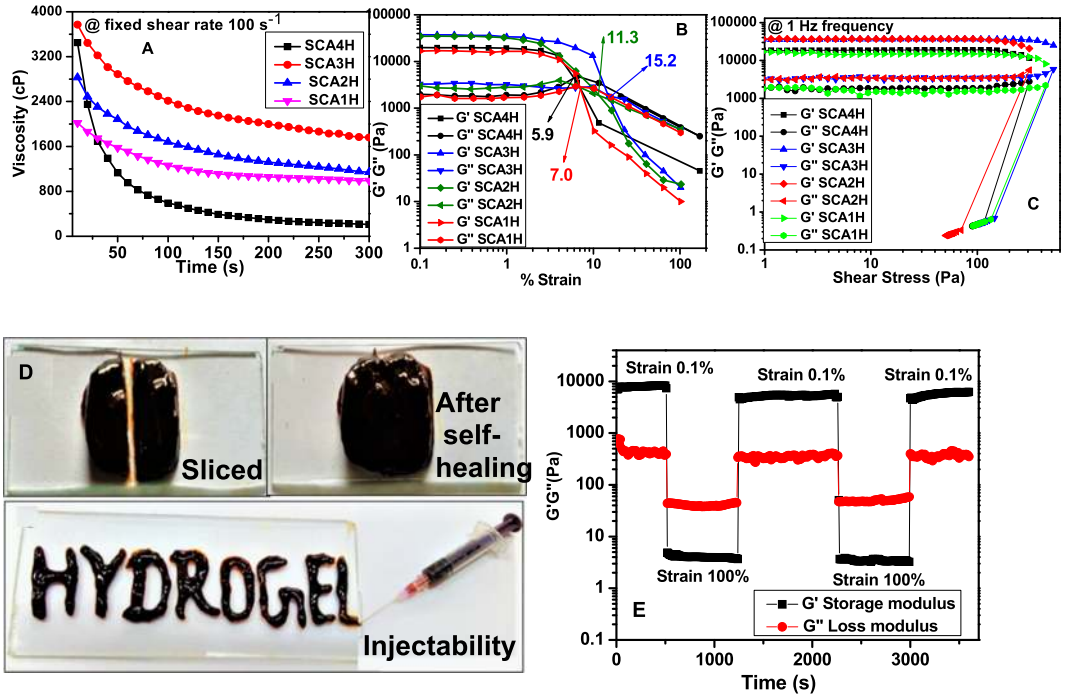

Figure 4. Viscoelastic measurements of SCA3H: viscosity vs time (panel A); G' and G'' vs % strain (panel B); G' and G'' vs shear stress (panel C); self-healing and injectability features of hydrogel (panel D); thixotropic measurement supporting self-healing (panel E).

hydrogel network. Upon decreasing the % strain, it again produced the hydrogel. The self-healing feature of the hydrogel is thus evidently manifested by thixotropic measurements in which several cycles could be repeated with time as a function of strain (Figure 4, panel E). It took about 700 s for healing. Such injectable and self-healing properties are significant for the healing of organism tissues in biomedical systems.

2.2.4. External Stimuli Responsiveness. The supramolecular nature of the as-synthesized hydrogel was further examined by investigating the effect of the external stimulus such as pH, temperature, and sonication. Interestingly, as-synthesized hydrogel exhibited reversible sol⇌gel transitions relatively in a narrow range of pH and temperature. The gelation starts at a pH of about 5.9 and gets fully converted at pH 7. Whereas, beyond a pH of 7.8 the sol formation is initiated and is completed at pH 9. The complete conversion of hydrogel into sol, however, occurs at pH 4.7 and 9.0 in the acidic and basic pH range, respectively (Figure 5, panel A). Even the sonication for a 5 min duration at a 50 Hz frequency led the conversion of gel into sol, which could be further assembled into gel upon cooling. The sonication essentially utilizes the physical force in the form of ultrasound waves causing to shear the supramolecular bond in the hydrogels resulting in its conversion into sol. These observations evidently demonstrate the as-synthesized hydrogel to be involving weak supramolecular interactions, which could be reversed by bringing a small variation in the physicochemical stimulus (pH, temperature, and sonication) (Figure 5, panel A; panel B; and panel C). The sol⇌gel transition as revealed by the thixotropic measurement also indicated the involvement of supramolecular interaction in the hydrogel (Figure 4, panel E).

2.2.5. Magnetic Study. M−H plots upon varying the temperature from 300 to 30 K clearly show that SCA3H exhibits superparamagnetic behavior, which shows the absence of any magnetic remanence (M_r) and coercivity (H_c) (Figure S4A,B; Table S6). Thereafter, a further decrease in the

Figure 5. SCA3H responsiveness for: pH (panel A); temperature (panel B); and sonication (panel C).

temperature showed a hysteresis loop suggesting a change in its magnetic behavior from superparamagnetic to ferromagnetic. The superparamagnetic behavior below blocking temperature has also been ascertained by recording its FC-ZFC curve (Figure S4C). In a control experiment, the M−H plot was also recorded for SCH at 300 K, which did not contain any Ag NPs (Figure S4D). A comparison of this M−H plot with SCA3H at 300 K exhibited the later to have slightly higher magnetization, which suggests that the presence of Ag NPs causes an increase in the magnetization in SCA3H. It is understood because of the possible orientation of the spin in β-FeOOH nanohybrids arising due to the binding of Ag through supramolecular interactions.

https://dx.doi.org/10.1021/acsomega.0c00815
ACS Omega 2020, 5, 13672−13684

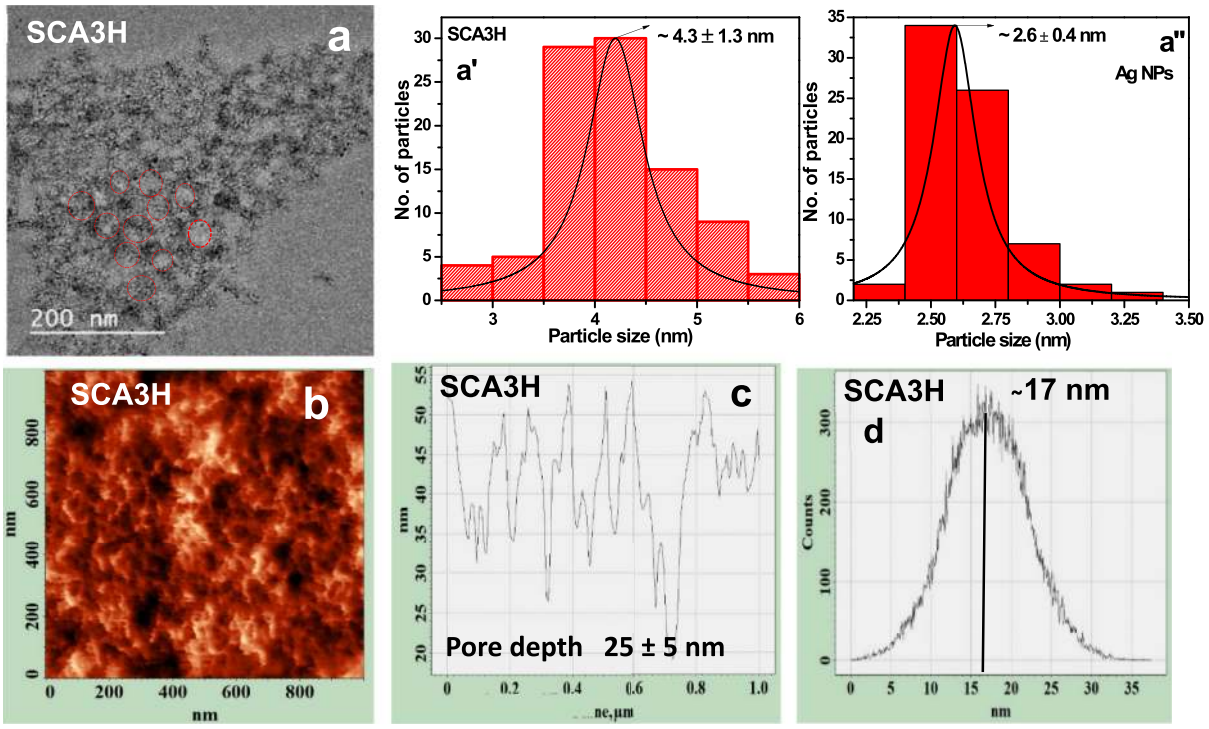

Figure 6. TEM micrograph of SCA3H (panel a); size distribution curve of β-FeOOH (panel a′); size distribution curve of Ag NPs (panel a″); AFM 2D image of SCA3H (panel b); pore depth analysis of SCA3H (panel c); roughness histogram of SCA3H (panel d).

2.2.6. Morphology. The morphology of SCA3H was examined by recording TEM, atomic force microscopy (AFM), and field-emission scanning electron microscopy (FESEM) (Figure 6, panel a, panel b, Figures S5A and S6), which showed the formation of a 3D network of porous hydrogels. An analysis of TEM micrographs recorded at lower magnification exhibited that the porous network consists of β-FeOOH nanoparticles decorated with Ag NPs, as was revealed by the SAED and HRTEM analysis (*vide ut supra*, Figure 1, panel d and panel e, Figure S5B). From various such TEM images, the size of β-FeOOH and Ag NPs have been estimated to be (nm): ~4.3 ± 1.3 and ~2.6 ± 0.4, respectively, and pore size has a size distribution ranging from about 10 to 24 nm with an average size of ~17.6 nm (Figure S5C) by the TEM image. From the analysis of the AFM image, the pore depth and surface roughness of the hydrogel were estimated to be ~25 ± 5 and ~17 nm, respectively (Figure 6, panel c and panel d). The adsorption isotherm for FD gel observed in BET measurements also showed the presence of both micro- and mesopores with an average size distribution (nm) of 1.2 and 6.6, respectively, giving a surface area of about 278 m^2 g^{-1} (Figure S7, Table S7).

3. APPLICATIONS

3.1. SERS Activity. Lately, hydrogel samples containing plasmonic NPs have been considered to provide the unique benefit of sensing Raman active biomolecules as well as the biological moieties when present in the microorganism.[38,39] In this reference, as-synthesized soft hydrogels, which could hold the analyte in its matrix, could be evaluated as a SERS substrate for their analysis in trace amounts.

In the present work, SERS activity of SCA3H has been explored for the detection of model drug MB. In these experiments, the concentration of MB was varied from 1 × 10^{-4} to 1 × 10^{-12} M (Figure 7). In order to evaluate the role of silver in enhancing the SERS activity, the Raman spectra of MB

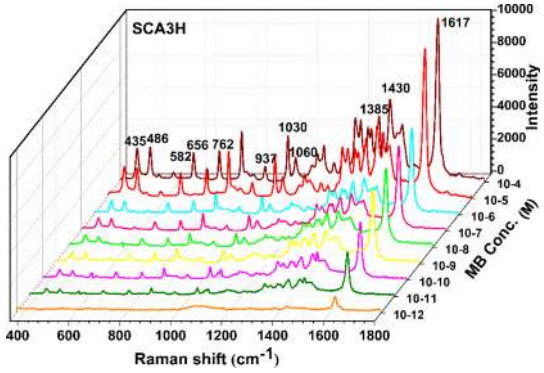

Figure 7. SERS of MB containing hydrogel (SCA3H) in the presence of Ag NPs.

were also recorded on the 5′-CMP mediated hydrogel (SCH) in the absence of Ag NPs (Figure S8a). In the entire concentration range, the Raman spectra exhibited bands (cm^{-1}) at 435, 486, 582, 656, 762, 937, 1030, 1060, 1385, 1430, and 1617 matching fairly well with the Raman spectrum of pure MB reported in the literature[40,41] as well as with its authentic sample recorded under identical experimental conditions (Figure S8b).

An examination of the Raman spectral data recorded in Figure 7 with that of in Figure S8a clearly shows that the presence of silver enhanced the intensity significantly without showing any appreciable change in the peak position, as compared to that of pure MB (Table S8). Specifically, a change in the SERS intensity in the presence of Ag NPs was higher for certain vibrational bands (cm^{-1}) of MB only *viz.* 486; 656,

https://dx.doi.org/10.1021/acsomega.0c00815
ACS Omega 2020, 5, 13672−13684

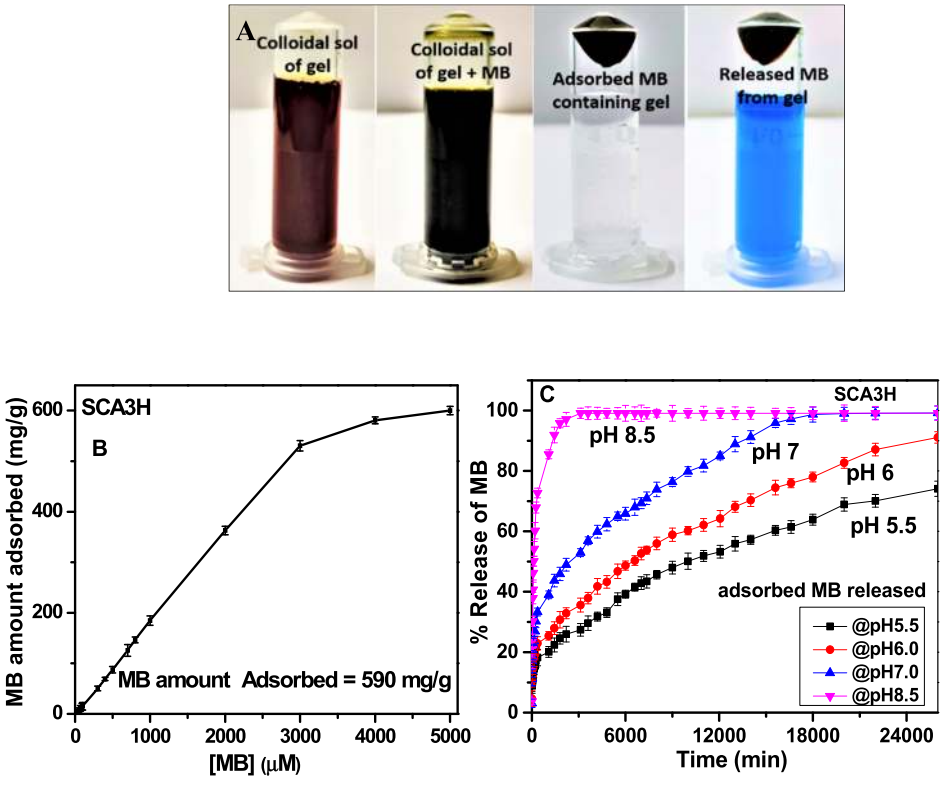

Figure 8. Digital images of MB adsorption and release from hydrogel (SCA3H) (panel A); adsorption curve of different amounts of MB on soft hydrogel (panel B); and % release of adsorbed MB amount at different pHs (panel C).

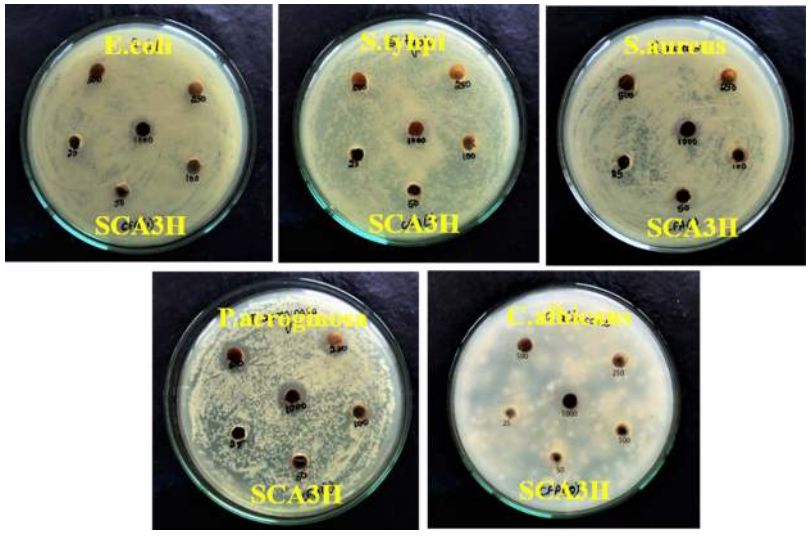

Figure 9. Antibacterial activity of SCA3H against different bacterial strains. (Photographs courtesy of BioGenics Research and training Center in Biotechnology Hubli, Karnataka, India.)

762/1030, and 1060 corresponding to the skeleton deformation of C−N−C; out-of-plane bending of C−H, and in-plane bending of C−H and C−N stretching functional groups. A comparison of the SERS spectrum of MB at its lower concentrations ($<10^{-10}$ M) on SCA3H to that of its spectrum in the absence of Ag NPs on the base matrix SCH clearly shows that the detection of MB in this concentration range was relatively poor for the later. Remarkably, MB could be detected at a significantly lower concentration ($\leq 10^{-12}$ M) on SCA3H. Moreover, the change in intensity becomes more prominent on SCA3H at relatively lower concentrations of MB, that is, below 10^{-10} M. The relative SERS enhancement factor is different for different peaks (Table S8). The difference is contributed by the polarization of different functional groups to a varied extent. The peak at 486 cm^{-1} arising due to the C−N−C group shows linearity in the lower concentration range only. From which the lower detection limit (LOD) has been estimated to be about 10^{-12} M (Figure S9). The observed enhancement in intensity might be contributed largely due to the chemical (CM) mechanism.[42,43] It may be mentioned that MB being an important molecule has been thoroughly explored for detection using SERS in solution elsewhere[44]

https://dx.doi.org/10.1021/acsomega.0c00815
ACS Omega 2020, 5, 13672−13684

but to the best of our knowledge this is the first report on the SERS detection of MB in the hydrogel sample.

3.2. Drug/Dye(s) Adsorption and Release Studies. As-synthesized hydrogel (SCA3H) was examined for the adsorption of cationic (MB) and anionic (MO) dye molecules. A varied amount of these dyes (3×10^{-5} to 5×10^{-3} M) was added to the colloidal solution of SCA3 and, thereafter, the pH was maintained at 7.0. Interestingly, the cationic dye MB exhibited a fairly high adsorption of 590 mg g^{-1} (Figure 8, panel B). On the other hand, the anionic dye (MO) did not show any appreciable adsorption (90 mg g^{-1}) (Figure S10A). The higher adsorption of cationic MB is also supported by the negative zeta potential observed for this hydrogel (Figure 1, panel b). Digital images of MB adsorption on hydrogel (SCA3H) and its release in water have been shown in Figure 8, panel A.

In order to examine the controlled drug delivery capability of as-synthesized hydrogel, the release of MB adsorbed (363 mg g^{-1}) on hydrogel (SCA3H) (Figure 8, panel B) was examined at different pH with time. The release experiments were designed at typical pHs: 5.5, 6.0, 7.0, and 8.5 and the respective % release profile of MB at these pH values (Figure 8, panel C). An examination of these curves shows that the release occurs rapidly at pH 8.5 and is almost over in about two days. However, the efficiency of release decreases regularly with a decrease in pH and followed the order (days): 8.5 (2) > 7.0 (12) > 6.0 (25) > 5.5 (32). Interestingly, at pH 7.0 the release is almost linear up to about 30−40% and was even higher at lower pHs. At lower pHs, it, however, took several days (~14 days) for complete release (Figure S10B). This might be possible due to the functional groups of 5′-CMP *viz.* NH^+, NH_3^+ O═ P−OH, and P−OH having varied pK_a values 4.5, 4.11, 6.3, and 0.8, respectively, thereby having different binding constants with MB. To the best of our knowledge, no such data is available on slow release and high loading of this drug.

3.3. Antibacterial Study. The antibacterial activity of as-synthesized hydrogel (SCA3H) was analyzed for Gram positive as well as Gram negative pathogenic bacterial strains using an agar disk diffusion assay (Figure 9, Table S9). The value of the minimum inhibitory concentration (in μg/mL) for these bacteria followed the order: *Pseudomonas aeruginosa* (250) < *Candida albicans* (500) < *Staphylococcus aureus* (500) < *Salmonella typhi* (1000) < *Escherichia coli* (1000).

For evaluating the role of Ag in affecting the antibacterial activity some control experiments were also designed against the same bacterial strains employing the SCH hydrogel (Figure S11; Table S10). A comparison of these data clearly shows that under the used experimental conditions, SCH did not demonstrate any antibacterial activity in contrast to that of SCA3H. Remarkably, the highest susceptibility is noted for *P. aeruginosa* (MDR). Detailed mechanism of the antibacterial activity is under investigation.

4. DISCUSSION

As-synthesized hydrogels consist of a solid-like network involving interactions among different functional groups of the building block(s) comprising 5′-CMP bound β-FeOOH coated by Ag NPs. The TEM micrographs and surface analysis of SCA3H by XPS clearly show the presence of Ag on the surface of β-FeOOH NPs in the hydrogel (Figure 1, panel e and Figure 2, panel A-b). This is evidenced by the lower magnification TEM image having smaller dark particles of Ag to be present on the lighter particles of the matrix at various locations (Figure S5A). Further, the effective gel formation takes place only in a specific concentration range of Ag (0.7−1.0 mM) at pH 7.0 and 37 °C (*vide supra*; Figure 1) in the self-assembly. Because any change in these conditions led to the poor gelation associated with the reduced stability (as was revealed by zeta and viscoelastic measurements, respectively (Figure 1, panel b, Table S1; Figure 4, Table S5), it evidently suggests that under optimized conditions, the hydrogel formation might be involving noncovalent interactions amongst the building blocks produced in SCA3 (Scheme 1A). At pH 7.0, SCA3 having a negatively charged hydrophilic head (5′-CMP molecule) in the shell and the hydrophobic components (β-FeOOH and Ag) as the core, it might be producing the anionic micelle-like structure. This hypothesis was probed by designing a DLS experiment, in which the hydrodynamic diameter (D_h) as well as intensity were monitored as a function of [Ag NPs]. From these plots, the critical micelle concentration (CMC) of this system is arrived to be at 1 mM of Ag NPs and corresponding to which the hydrodynamic radius comes out to be ~321 nm (Figure S12). The formation of gel at this concentration is also very well supported by the porous morphology observed in the TEM measurement (Figure 6, panel a; Scheme 1). Beyond this concentration, the hydrodynamic diameter and intensity showed a steep increase, which is understood because of an increase in the number of micelles. A similar micellar structure(s) involving supramolecular interactions among oligonucleotides and hydrophobic moieties are known to be present in the natural biological system(s).[45]

It is curious that the supramolecular interactions among these moieties occur only in the self-assembly to form hydrogel. It is likely that the micelles upon extensive interactions among themselves eventually produces gel-like structures in self-assembly creating the observed porous morphology in SCA3H. Such interactions are also indicated by the CD spectroscopic measurements, which showed a change in the chirality in the 5′-CMP in the hydrogel sample, as is understood by the puckering of the ribose sugar of 5′-CMP in SCA3H (Figure 2, panel B). The puckering causes a change in its conformation from C2′-endo to C3′-endo, enhancing various supramolecular interactions among 5′-CMP, β-FeOOH and Ag NPs. These interactions introduce new transitions involving various associated supramolecular structures and are also very well supported by IR and Raman spectroscopy (Figure 2, panel C and panel D). The increased stability of the gel structure in SCA3H is revealed by an increase in its LVR range and yield strain (Figure 4, panel B) as compared to that of SCH.[29]

The involvement of supramolecular interactions is clearly demonstrated experimentally under used experimental conditions by the observed multistimulus-responsive reversible transformation (Figure 5). The multistimulus-responsiveness to pH, temperature, and sonication may be understood based on the noncovalent interactions of inorganic phases (β-FeOOH and Ag) with different functional groups of 5′-CMP (NH^+, NH_3^+ O═P−OH and P−OH having varied pK_a as mentioned above (Scheme 1). Therefore, in different pH ranges, the intensity of binding interactions of 5′-CMP with Ag and iron oxide phase gets changed resulting in responsiveness. In view of these at lower and higher pH(s), the structure arrived in Scheme 1 under optimized conditions will undergo chemical transformation into different structures (Scheme S1).

https://dx.doi.org/10.1021/acsomega.0c00815
ACS Omega 2020, 5, 13672−13684

Silver-decorated β-FeOOH nanoparticles essentially provide more coordinating sites, in which silver and β-FeOOH bind through supramolecular interactions with each other as well as with the different functional groups of 5′-CMP as is manifested by the spectroscopic analysis (Figure 1, panel a; Figure 2, panel B, panel C, and panel D), thus assisting in an increase in solid-like networking required for gelation (Figure 4; Scheme 1). An increase in networking may thus be responsible for the observed enhancement in % swelling (Figure 3, curve a) and its multifunctional capabilities such as self-healing, injectability, and pH-responsive drug delivery (Figure 4, panel D and Figure 8, panel C). It essentially demonstrates that the as-synthesized hydrogels to be acting like a smart gel, which is also manifested by thixotropic measurements in which several cycles could be repeated with time as a function of strain (Figure 4, panel E).

The presence of Ag in the network of SCA3H introduces more active sites for the adsorption of the analyte, thereby resulting in a significant increase in its loading capabilities for model drug MB on its surface as compared to that of SCH. Based on the above observations, the interaction among different components in the hydrogels are shown in Scheme 1C.

In order to examine the contribution of the chemical mechanism (CM) toward the enhancement of SERS signals, some control experiments were designed by recording the IR spectra of adsorbed MB on the surface of SCH (SCHMB) and SCA3H (SCA3HMB) (Figure S13A). A comparison of these spectra clearly revealed relatively more prominent interactions of MB with SCA3H, causing a red shift in the peaks due to $[\nu_s(C-S-C)/\nu(C-N)/\delta(C-H)/\gamma(C-H)/\delta(C-S-C)/\delta_{het}(C-C))$, $(\delta_{het}(C-N))$, $(\nu_{het}(C=S^+))$, and $(\nu_{het}(C=N)/\nu_{het}(C=C)]$,[46] which suggested the occurrence of charge transfer from these functional groups of MB to Ag NPs involving the CM mechanism. These findings evidently revealed that the CM mechanism might be operating in enhancing SERS signals.

To the best of our knowledge, the present hydrogel synthesized from natural nucleotide (5′-CMP), depicted all desirable enhanced physicochemical features of supramolecular hydrogel to those reported earlier involving other nucleotides[31−33] (Table 1).

5. CONCLUSIONS

In summary, an *in situ* coating of Ag NPs on the surface of 5′-CMP-mediated akaganeite nanohybrids produces a building block, providing the new coordination sites for noncovalent interactions among the functionalities of 5′-CMP and β-FeOOH with Ag NPs, which promoted the fabrication of smart supramolecular hydrogel. The Ag centers in the structural network of the hydrogel acted as active site(s) to induce novel multifunctional features *viz*. % swelling, loading/release capabilities for the cationic drug/dye molecule, self-healing, injectability, exhibiting excellent SERS for MB-like drug molecule besides imparting them the interesting antibacterial features. The noncovalent bonding in the hydrogel is nicely manifested by the reversible sol⇌gel transformation under multistimulus-responsiveness to pH, temperature, and sonication in a narrow range of the respective parameters, making it a smart material.

Thus, the as-synthesized hydrogels consisting of greener components such as 5′-CMP, β-FeOOH, and Ag, prepared under physiological conditions of pH and temperature, provide a safe matrix, displaying distinctive multifunctional features of

Table 1. Comparison Table Exhibiting Different Physicochemical Properties of Ag NPs Decorated Nucleotide-Mediated Hydrogels[a]

nucleotide/in presence of	gelation time/pH	stimuli responsive/self-healing/injectability	swelling	loading (mg/g)	pH/%release/days	SERS	antibacterial	refs
5′-GMP (50 mM)/Ag^+	30 min/3.8−5	NR/NR/NR	NR	NR	NR	NR	NR	31
5′-AMP, (40 mM)/Ag^+	NR/4	NR/NR/NR	NR	NR	NR	NR	NR	32
5′-IMP (10 mM)/Ag^+	24 h / not specified	reported/reported/reported	NR	NR	NR	NR	reported	33
5′-CMP (2.5 mM)/Ag NPs	<5 min/7	reported/reported/reported	580%	590	8.5/98/2, 7/98/12, 6/98/25, 5.5/98/32	LOD (MB) 10^{-4} to 10^{-12} M	reported	present work

[a]NR denotes not reported, LOD denotes the limit of detection.

https://dx.doi.org/10.1021/acsomega.0c00815
ACS Omega 2020, 5, 13672−13684

supramolecular hydrogels with remarkably high loading/controlled-release of drug-like molecule(s), SERS behavior, and antibacterial properties.

6. EXPERIMENTAL SECTION

6.1. Reagents and Instruments Used. The analytical grade anhydrous $FeCl_3$ and KBr (Merck); cytidine 5′-monophosphate disodium salt (5′-CMP) (Alfa Aesar); $HClO_4$, phosphate buffered saline of pH 7.0 and glucose (HiMedia); NaOH (BDH); and silver nitrate (SRL), MB (Thomas Baker), and methyl orange (SRL) were purchased and used without further purification. The carbon coated copper grid of 200 mesh were purchased from M/s ICON analytical and dialysis tubing (seamless cellulose tubing/dialysis tubing closures) purchased from Sigma. All samples were prepared in Millipore water having 18.2 MΩ conductivity.

The electronic spectra measurements were performed on a PerkinElmer (model Lambda 950) UV−vis−NIR spectrophotometer. Co Kα line (1.78897 Å) was used to record the XRD patterns of the powder samples on a Rigaku X-ray diffractometer. An inVia Renishaw Raman spectrometer (serial no. 021R88 and H33197) equipped with a confocal microscope was used for recording the Raman spectrum of all the powder samples using Ar ion 514 nm laser source having a resolution of ±1 cm^{-1} and 2.5 μm confocal resolution. DLS measurements (zeta potential and hydrodynamic size) of the hydrogel samples were performed on a Malvern Instrument using 632 nm He−Ne laser as a light source. BET measurement of the powder sample was recorded on an Autosorb-iQ2 (Quanta chrome Instruments, USA at 77.77.350 K). XPS of the powder samples was performed on (PHI Versa Probe III electron spectrometer) using: source Al Kα 1486.708 keV, step width = 0.05 eV, energy resolution = 0.5 eV, pass energy = 55 eV at a base pressure of 10^{-7} mbar for the surface elemental study. The Fourier transform infrared (FTIR) spectra in the mid-IR range (1800−400 cm^{-1}) were recorded on a PerkinElmer (FTIR) spectrophotometer using KBr medium at 0.5 cm^{-1} resolution. The surface roughness was analyzed by using AFM in semi-contact mode purchased from NTEGRE (NTMDT). Field emission electron microscopy (Carl Zeiss) equipped with EDAX was used for the determination of surface morphology and elemental composition using 15 kV accelerating voltage. TEM images, SAED pattern, and HRTEM of the samples were recorded on a FEI Tecnai G^2 20 S-TWIN at 200 kV equipped with a CCD camera. A superconducting quantum interference device (Quantum Design MPMS-3) instrument was used for magnetic measurements. The magnetic behavior of the FD gel was measured by recording the magnetization as a function of the applied magnetic field of 1−7 T (M−H plots) at various temperatures using SQUID. The viscoelastic measurements of the hydrogel sample were performed on a MCR 102 rheometer purchased from Anton Paar using a cone—plate geometry having 40 mm diameter and 1° cone angle at 20 °C. A Chirascan spectropolarimeter acquired from Applied Photophysics, U.K, having a resolution of 1 nm was used for recording the circular dichroism (CD) spectrum of the colloidal samples. A silicon oil bath attached with a temperature controller (Medica instrument MFG., CO) was used for the reactions. An Eutech 510 pH meter was used to measure the pH of the samples. A REMI microprocessor research centrifuge (model PR-24) and Eppendorf centrifuge 5804 R were used for the centrifugation of the hydrogel samples at 8000 rpm for 20 min at RT.

6.2. Method of Synthesis. *6.2.1. In Situ Coating of Ag Nanoparticles on 5′-CMP-Capped β-FeOOH Nanohybrids (Ag-β-FeOOH@5′-CMP).* 5′-CMP molecule-mediated β-FeOOH nanohybrids have been synthesized following the previously reported colloidal approach.[29] The pH of the β-FeOOH@5′-CMP colloidal solution was maintained at 10.5 by using dilute NaOH (1×10^{-3} M). To 100 mL of this colloidal solution, a varied amount of silver nitrate (5×10^{-4} to 1.4×10^{-3} mM) was added under stirring and the resulting mixture was further stirred vigorously for about 20 min. To this colloidal solution, about 6 times [glucose] to that of [$AgNO_3$] was added at pH = 10.5 and this solution was stirred for about 15 min, followed by heating for 30 min at 50 °C under continuous stirring. In this reaction, glucose acts as a reducing agent causing the reduction of $AgNO_3$ to Ag NPs. For hydrogel formation, the pH of the colloidal solution containing the silver nanoparticles was adjusted at 7.0 by adding perchloric acid (1×10^{-3} M). The used abbreviation(s) for the colloidal solution and their respective hydrogels having different [Ag NPs] are: SCA1 (0.5 mM), SCA2 (0.7 mM), SCA3 (1 mM), and SCA4 (1.4 mM) and SCA1H (0.5 mM), SCA2H (0.7 mM), SCA3H (1 mM), and SCA4H (1.4 mM) respectively.

6.2.2. Sample Preparation for Various Studies. For optical, zeta potential, and circular dichroism measurements, the above referred samples were diluted about 10 times. IR, Raman, XRD, XPS, BET, and magnetic studies were performed on the respective lyophilized solid hydrogel samples. For AFM, FESEM, and TEM, the diluted samples were drop cast on a glass slide and carbon coated copper grid, respectively, and dried overnight in the dark in a desiccator. For BET measurements, the solid samples were degassed for 5 h at 105 °C. For rheological experiments, the hydrogels were centrifuged for 20 min at 5000 rpm at RT. For adsorption study, the dye/drug solution was shaken vigorously on a shaker at RT for about 30 min and left for equilibration for about 2 h. The hydrogel from the reaction mixture was separated by centrifugation.

For SERS measurements, a varied amount of MB in the concentration range of 1×10^{-12} to 1×10^{-4} M were dispersed in the SCA3H hydrogel. These samples were then shaken for 90 min at RT followed by its equilibration for 3 h for the adsorption of MB. In a control experiments, similar amounts of MB were dispersed on the base matrix SCH (which did not contain Ag NPs) and was further processed under identical conditions of experiments as followed for SCA3H. In each case, 50 μL of solution was drop cast on a glass slide and dried in a desiccator in dark at RT. The dried samples were subjected for the SERS measurements.

6.2.3. % Swelling. The % swelling of hydrogel was calculated using the following formula

$$\%\ \text{swelling} = \frac{W_s - W_D}{W_D} \times 100$$

W_s weight of swelled hydrogel and W_D = weight of dried hydrogel.

6.2.4. Dye(s) Adsorption and Release Studies. For adsorption studies, the 15 mL of colloidal solutions of hydrogel (165 mg/100 mL) were mixed with different amounts (0.03−5.0 mM) of MB and these samples were

https://dx.doi.org/10.1021/acsomega.0c00815
ACS Omega 2020, 5, 13672−13684

vigorously shaken on a water bath shaker for 60 min at RT and then kept for 2 h for equilibration. The amount of adsorbed/released dye was estimated by using UV−vis spectroscopy. For the release of adsorbed dye, the respective sample was brought in contact with water having different pH(s). The amount of released dye was estimated at different time intervals.

The amount of dye/drug molecule adsorbed by the hydrogels was calculated using the following formula: loading amount q_e (mg/g) = $\frac{(C_0 - C_t)}{m} \times V$,where C_0 (mg/L) = initial dye concentration, C_t (mg/L) = dye concentration at time t, V = volume of the dye solution (L), and m = weight of the adsorbent (g).

6.2.5. Antimicrobial Study. The antimicrobial activity of Ag coated β-FeOOH@5′-CMP hydrogel was performed by using agar disk-diffusion method. Initially, the stock cultures of both Gram positive (*S. aureus*) and Gram negative (*E. coli*, *S. typhi*, *P. aeruginosa*) and fungi (*C. albicans*) bacterial strain(s) were revived by inoculating in broth media and grown at 37 °C for 18 h. The agar plates of the above media were prepared and wells were made in the plate. Each plate was inoculated with 18 h old cultures (100 μL, 10^{-4} cfu) and spread evenly on the plate. After 20 min, the wells were filled with the sample at different volumes. All the plates were incubated at 37 °C for 24 h and the diameter of inhibition zone were noted.

■ ASSOCIATED CONTENT

Supporting Information

The Supporting Information is available free of charge at https://pubs.acs.org/doi/10.1021/acsomega.0c00815.

> UV−vis spectra of Ag NPs, XPS for P, C and Cl elements, viscoelastic measurement graphs, M−H curve at different temperatures, TEM images of SCA3H at lower magnification, pore size distribution graph of SCH3H, FESEM image and elemental mapping, BET graphs, Raman of pure MB and SERS of MB on SCH, SERS measurement for SCA3H, adsorption of MO and release curves of MB at different pH for a long time, antibacterial study of SCH, DLS measurements of hydrogels for CMC determination, IR spectra of pure MB, SCHMB, and SCA3HMB, table for zeta potential, XPS, IR data, Raman data, viscoelastic data, magnetization data, BET, SERS data, antibacterial study of SCA3H, and antibacterial study of SCH (PDF)

■ AUTHOR INFORMATION

Corresponding Author

Anil Kumar − *Department of Chemistry, Indian Institute of Technology Roorkee, Roorkee 247667, India;* orcid.org/0000-0003-1805-6603; Phone: +91 1332 285799; Email: anilkfcy@iitr.ac.in, akmshfcy@gmail.com; Fax: +91 1332 273560

Author

Priyanka − *Department of Chemistry, Indian Institute of Technology Roorkee, Roorkee 247667, India*

Complete contact information is available at: https://pubs.acs.org/10.1021/acsomega.0c00815

Author Contributions

The manuscript was written through equal contributions of both authors. Both authors have given approval to the final version of the manuscript.

Notes

The authors declare no competing financial interest.

■ ACKNOWLEDGMENTS

The financial support of IIT Roorkee, Roorkee to AK (grant no. GCF-004-EFMC-01-414) to undertake this work is gratefully acknowledged. Priyanka is thankful to MHRD, New Delhi for awarding SRF. We thank the Heads of IIC and MMED for providing me the facilities of XRD, AFM, TEM, and SQUID. Thanks are also due to BioGenics Research and Training Centre in Biotechnology Hubli, Karnataka, India for performing the antibacterial experiments.

■ REFERENCES

(1) Willner, I. Stimuli-Controlled Hydrogels and Their Applications. *Acc. Chem. Res.* **2017**, *50*, 657−658.

(2) Tang, L.; Liao, S.; Qu, J. Self-Healing and Multistimuli-Responsive Hydrogels Formed via a Cooperation Strategy and Their Application in Detecting Biogenic Amines. *ACS Appl. Mater. Interfaces* **2018**, *10*, 27365−27373.

(3) Saunders, L.; Ma, P. X. Self-Healing Supramolecular Hydrogels for Tissue Engineering Applications. *Macromol. Biosci.* **2019**, *19*, 1800313.

(4) Wang, L.; Shi, X.; Wu, Y.; Zhang, J.; Zhu, Y.; Wang, J. A Multifunctional Supramolecular Hydrogel: Preparation, Properties and Molecular Assembly. *Soft Matter* **2018**, *14*, 566−573.

(5) Dong, R.; Pang, Y.; Su, Y.; Zhu, X. Supramolecular Hydrogels: Synthesis, Properties and Their Biomedical Applications. *Biomater. Sci.* **2015**, *3*, 937.

(6) Du, X.; Zhou, J.; Shi, J.; Xu, B. Supramolecular Hydrogelators and Hydrogels: From Soft Matter to Molecular Biomaterials. *Chem. Rev.* **2015**, *115*, 13165−13307.

(7) Appel, E. A.; del Barrio, J.; Loh, X. J.; Scherman, O. A. Supramolecular Polymeric Hydrogels. *Chem. Soc. Rev.* **2012**, *41*, 6195−6214.

(8) Draper, E. R.; Adams, D. J. Low-Molecular-Weight Gels: The State of the Art. *Chem* **2017**, *3*, 390−410.

(9) Christoff-Tempesta, T.; Lew, A.; Ortony, J. Beyond Covalent Crosslinks: Applications of Supramolecular Gels. *Gels* **2018**, *4*, 40.

(10) Zhang, L.; Jean, S. R.; Ahmed, S.; Aldridge, P. M.; Li, X.; Fan, F.; Sargent, E. H.; Kelley, S. O. Multifunctional Quantum Dot DNA Hydrogels. *Nat. Commun.* **2017**, *8*, 381.

(11) Chen, M.-L.; Shen, L.-M.; Chen, S.; Wang, H.; Chen, X.-W.; Wang, J.-H. In situ growth of β-FeOOH nanorods on graphene oxide with ultra-high relaxivity for in vivo magnetic resonance imaging and cancer therapy. *J. Mater. Chem. B* **2013**, *1*, 2582−2589.

(12) Zeng, L.; Ren, W.; Zheng, J.; Wu, A.; Cui, P. Synthesis of water-soluble FeOOH nanospindles and their performance for magnetic resonance imaging. *Appl. Surf. Sci.* **2012**, *258*, 2570−2575.

(13) Kumar, A.; Gupta, S. K. 5′-Guanosine Monophosphate Mediated Biocompatible Porous Hydrogel of β-FeOOH-Viscoelastic Behavior, Loading, and Release Capabilities of Freeze-Dried Gel. *J. Phys. Chem. B* **2014**, *118*, 10543−10551.

(14) Shi, G.; Chen, W.; Zhang, Y.; Dai, X.; Zhang, X.; Wu, Z. An Antifouling Hydrogel Containing Silver Nanoparticles for Modulating the Therapeutic Immune Response in Chronic Wound Healing. *Langmuir* **2019**, *35*, 1837−1845.

(15) Lengert, E.; Yashchenok, A. M.; Atkin, V.; Lapanje, A.; Gorin, D. A.; Sukhorukov, G. B.; Parakhonskiy, B. V. Hollow Silver Alginate Microspheres for Drug Delivery and Surface Enhanced Raman Scattering Detection. *RSC Adv.* **2016**, *6*, 20447−20452.

(16) Fateixa, S.; Daniel-da-Silva, A. L.; Nogueira, H. I. S.; Trindade, T. Raman Signal Enhancement Dependence on the Gel Strength of

Ag/Hydrogels Used as SERS Substrates. *J. Phys. Chem. C* **2014**, *118*, 10384−10392.
(17) Yang, L.; Li, P.; Liu, J. Progress in Multifunctional Surface-Enhanced Raman Scattering Substrate for Detection. *RSC Adv.* **2014**, *4*, 49635−49646.
(18) Raiten, D. J.; Talbot, J. M.; Waters, J. H. Assessment of nutrient requirements for infant formulas. *J. Nutr.* **1998**, *128*, 2059S−2293S.
(19) Kumar, A.; Kumar, V. Biotemplated Inorganic Nanostructures: Supramolecular Directed Nanosystems of Semiconductor(s)/Metal(s) Mediated by Nucleic Acids and Their Properties. *Chem. Rev.* **2014**, *114*, 7044−7078.
(20) Hodgson, D. R. W. Physicochemical Aspects of Aqueous and Nonaqueous Approaches to the Preparation of Nucleosides, Nucleotides and Phosphate Ester Mimics. *Adv. Phys. Org. Chem.* **2017**, *51*, 187−219.
(21) Zhou, P.; Yao, J. F.; Sheng, C. F.; Li, H. A Continuing Tale of Chirality: Metal Coordination Extended Axial Chirality of 4, 4'-Bipy to 1D Infinite Chain Under Cooperation of a Nucleotide Ligand. *CrystEngComm* **2013**, *15*, 8430−8436.
(22) Aoki, K.; Saenger, W. Heavy metal ion interactions with deoxy nucleotides. X-ray crystal structures of orthorhombic and monoclinic forms of 2'-deoxy cytidine 5'-monophosphate complexed with Cd(II). *J. Inorg. Biochem.* **1984**, *20*, 225−245.
(23) Peters, G. M.; Davis, J. T. Supramolecular Gels Made from Nucleobase, Nucleoside and Nucleotide Analogs. *Chem. Soc. Rev.* **2016**, *45*, 3188−3206.
(24) Pu, F.; Ren, J.; Qu, X. Nucleobases, Nucleosides, and Nucleotides: Versatile Biomolecules for Generating Functional Nanomaterials. *Chem. Soc. Rev.* **2018**, *47*, 1285−1306.
(25) Liu, Y.; Hsu, S.-h. Synthesis and Biomedical Applications of Self-healing Hydrogels. *Front. Chem.* **2018**, *6*, 449.
(26) Xu, L.; Zhang, Z.; Fang, X.; Liu, Y.; Liu, B.; Liu, J. Robust Hydrogels from Lanthanide Nucleotide Coordination with Evolving Nanostructures for a Highly Stable Protein Encapsulation. *ACS Appl. Mater. Interfaces* **2018**, *10*, 14321−14330.
(27) Liang, H.; Zhang, Z.; Yuan, Q.; Liu, J. Self-Healing Metal-Coordinated Hydrogels Using Nucleotide Ligands. *Chem. Commun.* **2015**, *51*, 15196−15199.
(28) Kumar, A.; Gupta, S. K. 5′-Guanosine Monophosphate Mediated Biocompatible Porous Hydrogel of *β*-FeOOH-Viscoelastic Behavior, Loading, and Release Capabilities of Freeze-Dried Gel. *J. Phys. Chem. B* **2014**, *118*, 10543−10551.
(29) Kumar, A.; Priyanka, P. Environmentally benign pH-responsive cytidine-5′-monophosphate molecule-mediated akaganeite (5′-CMP-*β*-FeOOH) soft supramolecular hydrogels induced by the puckering of ribose sugar with efficient loading/release capabilities. *New J. Chem.* **2019**, *43*, 14997−15013.
(30) Rodríguez-Llansola, F.; Escuder, B.; Miravet, J. F.; Hermida-Merino, D.; Hamley, I. W.; Cardin, C. J.; Hayes, W. Selective and Highly Efficient Dye Scavenging by a pH-Responsive Molecular Hydrogelator. *Chem. Commun.* **2010**, *46*, 7960−7962.
(31) Dash, J.; Patil, A. J.; Das, R. N.; Dowdall, F. L.; Mann, S. Supramolecular hydrogels derived from silver ion-mediated self-assembly of 5′-guanosine monophosphate. *Soft Matter* **2011**, *7*, 8120−8126.
(32) Hu, Y.; Xie, D.; Wu, Y.; Lin, N.; Song, A.; Hao, J. Hydrogels Based on Ag^{+}-Modulated-Assembly of 5'-Adenosine Monophosphate for Enriching Biomolecule, Chem. *Chem.—Eur. J.* **2017**, *23*, 15721−15728.
(33) Thakur, N.; Sharma, B.; Bishnoi, S.; Mishra, S. K.; Nayak, D.; Kumar, A.; Sarma, T. K. Multifunctional Inosine Monophosphate Coordinated Metal-Organic Hydrogel: Multistimuli Responsiveness, Self-Healing Properties, and Separation of Water from Organic Solvents. *ACS Sustainable Chem. Eng.* **2018**, *6*, 8659−8671.
(34) Sun, B.; Barnard, A. S. The Impact of Size and Shape Distributions on the Electron Charge Transfer Properties of Silver Nanoparticles. *Nanoscale* **2017**, *9*, 12698−12708.
(35) Wagner, C. D.; Riggs, W. M.; Davis, L. E.; Moulder, J. F.; Mouilenberg, G. E. *XPS Handbook of X-Ray Photoelectron Spectroscopy*; Perkin-Elmer Corporation: Minnesota, 1969, Vol. *112*.
(36) Qiu, Q.-m.; Zhou, P.; Gu, L.; Hao, L.; Liu, M.; Li, H. Cytosine-Cytosine Base-Pair Mismatch and Chirality in Nucleotide Supramolecular Coordination Complexes. *Chem.—Eur. J.* **2017**, *23*, 7201−7206.
(37) Mathlouthi, M.; Seuvre, A. M.; Koenig, J. L. F.T.-I.R. and laser-raman spectra of cytosine and cytidine. *Carbohydr. Res.* **1986**, *146*, 1−13.
(38) Fateixa, S.; Nogueira, H. I. S.; Trindade, T. Hybrid Nanostructures for SERS: Materials Development and Chemical Detection. *Phys. Chem. Chem. Phys.* **2015**, *17*, 21046−21071.
(39) Mosier-Boss, P. Review on SERS of Bacteria. *Biosensors* **2017**, *7*, 51.
(40) Singh, N.; Prakash, J.; Misra, M.; Sharma, A.; Gupta, R. K. Dual Functional Ta-Doped Electrospun TiO_2 Nanofibers with Enhanced Photocatalysis and SERS Detection for Organic Compounds. *ACS Appl. Mater. Interfaces* **2017**, *9*, 28495−28507.
(41) Xiao, G.-N.; Man, S.-Q. Surface-enhanced Raman Scattering of Methylene Blue Adsorbed on Cap-Shaped Silver Nanoparticles. *Chem. Phys. Lett.* **2007**, *447*, 305−309.
(42) Le Ru, E. C.; Blackie, E.; Meyer, M.; Etchegoin, P. G. Surface Enhanced Raman Scattering Enhancement Factors: A Comprehensive Study. *J. Phys. Chem. C* **2007**, *111*, 13794−13803.
(43) Lum, W.; Bruzas, I.; Gorunmez, Z.; Unser, S.; Beck, T.; Sagle, L. Novel Liposome-Based Surface-Enhanced Raman Spectroscopy (SERS) Substrate. *J. Phys. Chem. Lett.* **2017**, *8*, 2639−2646.
(44) Lee, H. K.; Lee, Y. H.; Koh, C. S. L.; Phan-Quang, G. C.; Han, X.; Lay, C. L.; Sim, H. Y. F.; Kao, Y.-C.; An, Q.; Ling, X. Y. Designing surface-enhanced Raman scattering (SERS) platforms beyond hotspot engineering: emerging opportunities in analyte manipulations and hybrid materials. *Chem. Soc. Rev.* **2019**, *48*, 731−756.
(45) Wang, Y.; Wu, C.; Chen, T.; Sun, H.; Cansiz, S.; Zhang, L.; Cui, C.; Hou, W.; Wu, Y.; Wan, S.; Cai, R.; Liu, Y.; Sumerlin, B. S.; Zhang, X.; Tan, W. DNA Micelle Flares: A Study of the Basic Properties that contribute to Enhanced Stability and Binding Affinity in Complex Biological Systems. *Chem. Sci.* **2016**, *7*, 6041−6049.
(46) Ovchinnikov, O. V.; Evtukhova, A. V.; Kondratenko, T. S.; Smirnov, M. S.; Khokhlov, V. Y.; Erina, O. V. Manifestation of Intermolecular Interactions in FTIR Spectra of Methylene Blue Molecules. *Vib. Spectrosc.* **2016**, *86*, 181−189.

https://dx.doi.org/10.1021/acsomega.0c00815
ACS Omega 2020, 5, 13672−13684